SUPPLEMENT

DYNAMICS AND CHEMISTRY OF MARINE STRATOCUMULUS—DYCOMS-II

Flight Summaries

BY BJORN STEVENS, DONALD H. LENSCHOW, GABOR VALI, HERMANN GERBER, A. BANDY, B. BLOMQUIST, J.-L. BRENGUIER, C. S. BRETHERTON, F. BURNET, T. CAMPOS, S. CHAI, I. FALOONA, D. FRIESEN, S. HAIMOV, K. LAURSEN, D. K. LILLY, S. M. LOEHRER, SZYMON P. MALINOWSKI, B. MORLEY, M. D. PETTERS, D. C. ROGERS, L. RUSSELL, V. SAVIC-JOVCIC, J. R. SNIDER, D. STRAUB, MARCIN J. SZUMOWSKI, H. TAKAGI, D. C. THORNTON, M. TSCHUDI, C. TWOHY, M. WETZEL, AND M. C. VAN ZANTEN

This document is a supplement to "Dynamics and Chemistry of Marine Stratocumulus—DYCOMS-II," by Bjorn Stevens (*Bull. Amer. Meteor. Soc.*, **84,** 579–593) • © 2003 American Meteorological Society • *Corresponding author:* Bjorn Stevens, Dept. of Atmospheric Sciences, University of California, Los Angeles, 405 Hilgard Ave., Box 951565, Los Angeles, CA 90095-1565 • E-mail: bstevens@atmos.ucla.edu • DOI: 10.1175/BAMS-84-5-Stevens.

The experiment consisted of two basic flight patterns: entrainment and radar flight patterns. The entrainment flight patterns had a twofold objective: to measure divergence and turbulent fluxes at various levels and characterize the mean states of both the boundary layer and the overlying air column. To achieve these objectives, the basic entrainment flight plan consisted of stacks of 30-min (approximately 60-km diameter) circles. In contrast the objective of the radar flights was to characterize the evolution of a specific convective cell. For this reason, the radar flights consisted of shorter (6 min) legs that attempted to fly over or through a specific point in the flow along varied headings.

These differences between the two types of flight patterns are shown in Fig. S1. There were only two

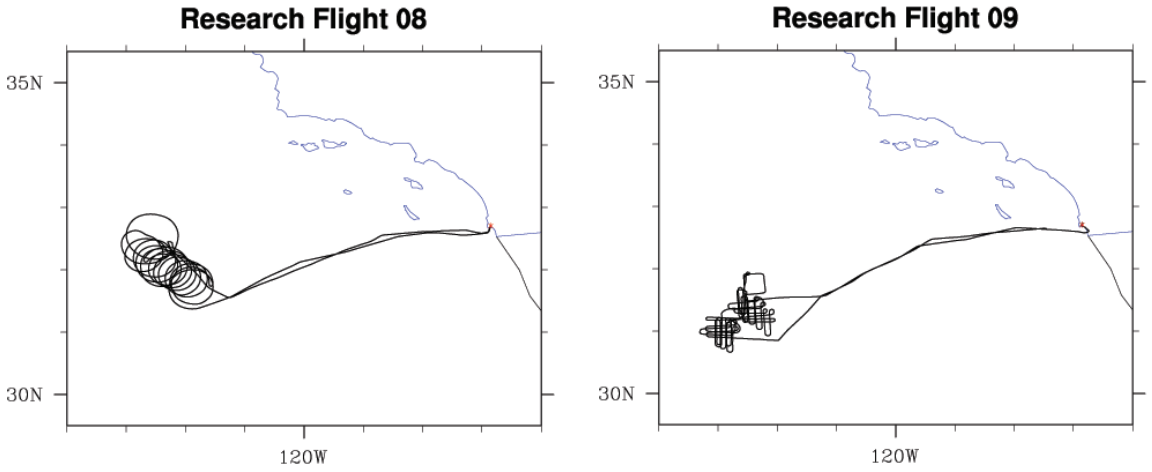

FIG. S1. Flight tracks for RF08 and RF09; note the center of the circles drift with the mean northwesterly winds.

radar flights, RF06 and RF09, and although the flight tracks were not identical between the two, the idea was similar. The general nature of all the entrainment flights was identical, the only difference being in the ordering of the legs, and the transitions between circles. In general two opposing circles[1] were flown consecutively at each altitude, thus yielding an hour at any given level. On some flights, however, either the subcloud or surface layer circles were performed in only one direction in order to make time for other maneuvers. In addition, the entrainment flights allowed time for one leg whose objective was determined on a flight-by-flight basis. Typically this leg was a porpoising maneuver to obtain numerous penetrations through the entrainment region at cloud top. Last, flight maneuvers for calibrating air motion sensing were performed twice during the experiment: once on the third test flight, which took place on station during the day on 7 July 2001, and once on the outbound ferry of RF07. The remainder of this summary focuses on the entrainment flight plans.

Figure S2 illustrates how legs and profiles were distributed in the time–height plane. The circular legs are annotated and described in Table S1. Although none of the entrainment flights followed this plan exactly, the essential elements were conducted on each flight. Flights differed in the ordering, heading sequence, and duration of the level legs; the exact position of the soundings; and the nature or the existence of the optional leg (which in the figure is indicated as a see-sawing, or porpoising, leg that repeatedly profiles the cloud-top region). But each flight had four flux legs of at least 30 min at roughly the indicated heights, three radar/lidar legs at approximately the indicated heights, and from four to five soundings dispersed throughout the time in the study area.

A basic summary of the conditions encountered on each flight is included in Table S2. Because the time on target approached 7 h, and the flight legs generally drifted with the mean wind (e.g., see the evolution of consecutive circles in Fig. S1), the actual area sampled by the aircraft was approximately 3000 km^2. For measurements of sea surface temperatures (SSTs), which were taken from the surface legs flown near the end of the time in the study area, this leads to a systematic high bias. For other quantities, the means can mask considerable time variability; this was perhaps most important for estimates of cloud base, which on some flights changed systematically through the course of the time in the study area by as much as 150 m. Among the flights the depth of the stratocumulus-topped boundary layer (STBL) varied by nearly a factor of 2, with similar variations in cloud-liquid water, cloud thickness, and wind speeds. Precipitation, as measured by the maximum radar reflectivity, was even more varied, with cloud layers ranging from essentially non- ($Z < -15$ dBZ) to heavily (at least for stratocumulus, i.e., $Z > 0$ dBZ) precipitating.

For reference in analyzing the flight data the time offsets (time in seconds from the beginning of the data record) for the level legs and soundings are tabulated for the seven entrainment flights are presented in

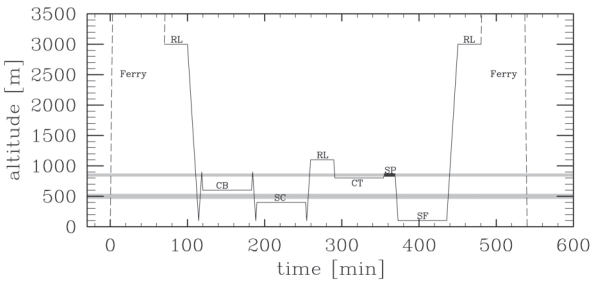

FIG. S2. Time–height cross section for basic entrainment flight plan. Approximately 410 min are spent in the target area. Shaded bars denote cloud top and base.

TABLE S1. Description of flight legs in basic entrainment flight plan. Here CW denotes a clockwise circle, CCW a counterclockwise circle.

Leg	Duration (min)	Heading	Description
RL1	30	CW	Radar/lidar and dropsonde leg at 3 km
CB	60	CW-CCW	Level flux leg just above cloud base (CB)
SC	60	CCW-CW	Level flux leg in subcloud (SC) layer
RL2	30	CW	Radar/lidar leg just above lidar dead zone
CT	60	CW-CCW	level flux leg just below cloud top (CT)
SP	30	CCW	Special (SP) leg, generally porpoising at cloud top
SF	60	CCW-CW	Surface (SF) leg at lowest safe flight level
RL3	30	CCW	Radar/lidar and dropsonde leg at 3 km

[1] Circles were flown by changing the aircraft heading at a constant rate in time, 12° min^{-1} for 30-min circles, thus defining circles with respect to the mean flow.

Tables S3–S6. Satellite conditions as observed from the Geostationary Operational Environmental Satellite (GOES) for the nine flights are shown in Fig. S3. Snapshots in this figure are from the end of each flight for the nocturnal, and at the beginning of each flight for the diurnal flights. Note the generally widespread uniform marine stratocumulus cloud cover.

INSTRUMENTATION. Another very important component of the second Dynamics and Chemistry of Marine Stratocumulus (DYCOMS-II) experiment strategy was the instrument package. Excepting remotely sensed data from satellites, and other data of opportunity, all the instrumentation was carried by a single platform—the National Science Foundation/National Center for Atmospheric Research (NSF/NCAR) C130. The placement of various instruments or inlets on the aircraft is illustrated in Figs. S4 and S5. Unless otherwise stated, all instruments recorded their measurements on the primary aircraft data system, thus ensuring precise temporal synchronization. The performance and details of these instruments is discussed further below.

Wind and turbulence measurement. The NCAR C130 incorporates three primary systems into the measurement of a three-dimensional wind vector:

- the inertial reference system (IRS) measures attitude angles (pitch, roll and yaw, or azimuth), accelerations, and position of the aircraft in an earth-based reference frame;
- the global positioning system (GPS) receiver measures the aircraft velocity and position in an earth-

Table S2. Summary of DYCOMS-II flights, Jul 2001. State variables are estimated from subcloud legs; SSTs are estimated from radiometric measurements during low-altitude (< 100 m) surface legs. Cloud base taken from average LCL for all legs within PBL. The cloud-top liquid-water $q_{l,max}$ is estimated from soundings. Flight latitude and longitude is at the center of flight region for middle 4 h on target.

Flight	1	2	3	4	5	6	7	8	9
Takeoff (UTC)[a]	0601	0624	0618	0622	0619	0539	0553	1945	1816
Landing	1518	1553	1546	1532	1541	1513	1549	0521	0345
Date[b] (Jul 2001)	10	11	13	17	18	20	24	25	27
Lat (°)	31.3	31.4	31.0	29.7	30.5	30.6	31.3	32.1	31.2
Lon (°)	–121.7	–121.7	–121.6	–121.5	–121.7	–122.0	–121.4	–122.4	–122.7
SST (°C)	19	19	19	20	19	N/A	19	18	N/A
Wind speed (m s^{-1})	8	8	12	6	10	8	7	5	5
Wind direction (°N)	324	310	300	274	287	340	326	319	345
Cloud top (m)	850	800	700	1075	925	600	825	600	600
Cloud base (m)	585	440	310	610	650	200	310	270	300
$\overline{\theta_l}$(K)	289	288	288	289	288	288	288	289	288
$\overline{q_t}$ (g kg^{-1})	9	9	10	9	8	9	10	10	10
$\overline{q_{l,max}}$ (g kg^{-1})	0.6	0.6	0.7	0.9	0.6	0.7	0.9	0.6	0.6
N (cm^{-3})[c]	148	59	207	168	151	100	116	110	165
CCN[d] (cm^{-3})	$106s^{0.4}$	$60s^{0.2}$	$300s^{0.8}$	$210s^{0.3}$	$210s^{0.3}$	$180s^{0.5}$	$140s^{0.4}$	$130s^{0.4}$	$290s^{0.3}$
CN (cm^{-3})	274	290	472	290	417	389	281	245	558

[a]Local time (Pacific daylight time, PDT) plus 7 h.

[b]At takeoff.

[c]For flights RF01 and RF02 these numbers are taken from SSP-100, for flights RF03–RF09 they are based on data taken with the FFSSP.

[d]The coefficients in this expression are derived by fitting data from a static CCN instrument to the form $N = Cs^k$. Relative errors in C and k are ±25% and ±35%, respectively.

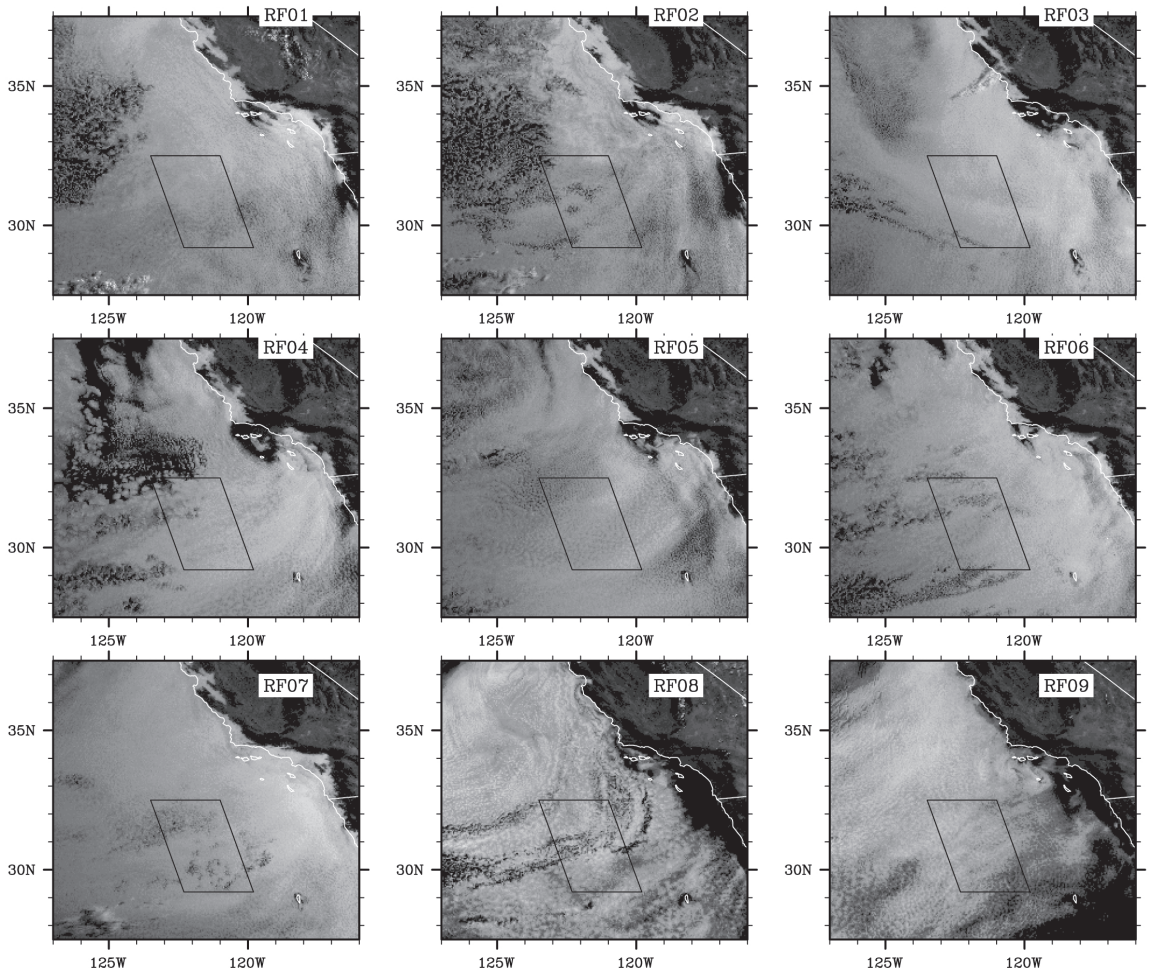

FIG. S3. GOES visible imagery for DYCOMS-II research flights.

based coordinate system using a constellation of satellites;

- the "radome gust probe" measures the air flow velocity relative to the aircraft using a cruciform array of five pressure ports on the C130 nose radome coupled to differential and absolute pressure sensors.

The air flow velocity measured relative to the aircraft coordinate system is combined with the motion of the aircraft relative to the earth coordinate system to yield a three-dimensional wind vector in meteorological coordinates. The mechanization equations and coordinate transformation matrices are detailed in Lenschow (1972, 1986).

INERTIAL REFERENCE SYSTEM. The C130 uses a Honeywell Laseref II SM strapdown ring laser gyro IRS (Kayton and Fried 1997) mounted in the cabin near fuselage station 240. The IRS provides position (latitude, longitude) initial accuracy of 0.8 n mi (with increasing uncertainty by 0.8 n mi h^{-1} hereafter), and pitch and roll accuracy to 0.05° rms and azimuth (true heading) accuracy of 0.4° rms. The primary source of error is the Schuler oscillation, a slowly varying drift in position and velocity measurements with a period of 84 min. The IRS has excellent short-term relative accuracy and resolution and its measurements are combined with the GPS, which has excellent absolute accuracy to provide a high-resolution, high-rate absolute accuracy measurement of aircraft position and velocity.

RADOME GUST PROBE. The radome gust probe measures the attack and sideslip (incident) flow angles relative to the aircraft and the dynamic pressure used in calculating the aircraft true airspeed. Five small pressure taps are drilled into the existing radome and tubing is routed to pressure transducers. The radome system (Brown et al. 1983), once calibrated for a specific aircraft, makes high-accuracy wind and turbulence measurements at scales larger than the characteristic dimension of the aircraft. In the case of the C130, the relevant

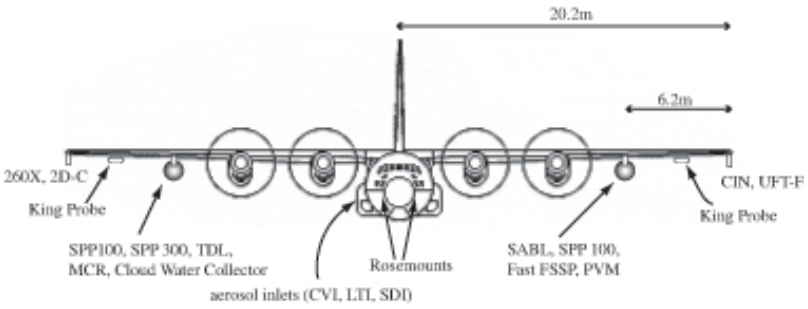

Fig. S4. Front view of C130 and probe locations.

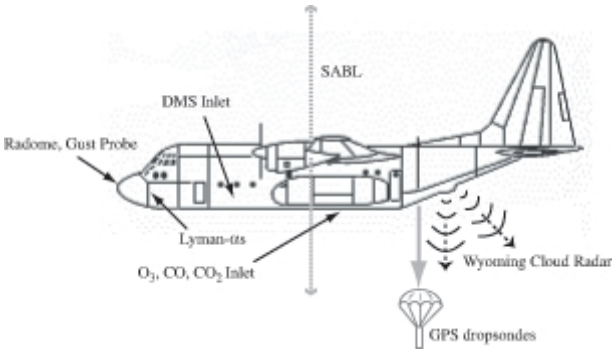

Fig. S5. Side view of C130.

scale value is the fuselage diameter, which measures 3.5 m.

Global positioning system receiver. The C130 uses a Trimble TANS III six-channel GPS receiver that provides measurements of aircraft position, velocity, and time at a 1-s update rate. The accuracies of the measurements are 16-m rms horizontal, 25-m rms vertical and 0.25 m s^{-1} for the velocities. Principles of the NAVSTAR GPS navigation can be found in Kayton and Fried (1997).

Temperature measurements. Rosemount total temperature probes. The NCAR C130 has two Rosemount model 102EAL total temperature probes and one Rosemount 102DB1CB deiced total temperature probe. These are platinum resistance wire probes with a nominal resistance of 50 Ω at 0°C. "Total temperature" refers to the temperature measured when the air is brought to rest without the removal or addition of any heat. The housing for the platinum element is designed to be in the airstream and to slow the air to achieve the maximum temperature rise due to adiabatic heating. The degree to which a sensor measures the total temperature is called the recovery factor. An ideal sensor has a recovery factor of 1.00. For the NCAR C130 probes it is 0.95. For the deiced temperature probe there is an additional correction of 0.2°C at sea level due to the deicing heat. Total temperature is relatively insensitive to location on the aircraft as long as it is outside the aircraft boundary layer (Cooper and Rogers 1991).

Sensor wetting in clouds and precipitation affect temperature sensor accuracy. At times the sensor is only partially wet so a correction as depicted by a wet-adiabatic process becomes questionable, and at 100 m s^{-1} the difference can be as much as 2°C between wet- and dry-bulb temperatures in a saturated environment (Lenschow and Pennell 1974). Another potential problem in the marine boundary layer is the accumulation of sea salt on the sensor element (Friehe 1986).

The accuracy of these probes is better than 0.5°C in cloud-free air as demonstrated by aircraft intercomparisons and tower fly-by calibrations. An "airspeed maneuver" where the aircraft airspeed is varied over the range of research airspeeds while maintaining altitude can also be used to estimate and verify the errors and corrections due to heating effects. The frequency response is less than 10 Hz (Spyers-Duran and Baumgardner 1983). (Corrections for dynamic heating and deicing are described online at http://raf.atd.ucar.edu/Bulletins/bulletins.html.)

The location of the Rosemount temperature probes is depicted in Fig. S4. The deiced probe (not shown) is just outboard of the left pod underneath the wing about 10 in. from the leading edge.

UFT. A specially designed version of the ultrafast thermometer (UFT-F; Haman et al. 1997) with two temperature sensors was prepared by DYCOMS-II. The UFT is a platinum resistance thermometer shielded from cloud drops by an upstream obstacle and strengthened by a tungsten coating. An advantage of the UFT-F is that it allows measurements of temperature at centimeter resolution (time constant about 10^{-4} s, signal recorded at 1 kHz, and selected segments recorded at 10 kHz). The UFT-F was originally to be mounted under the pod on the left wing of the NCAR C130 aircraft, close to the fast forward scattering spectrometer probe (FFSSP) and particle volume monitor (PVM) probes; due to technical limitations the probe had to be moved to the tip of the left wing, 6 m from the other fast probes. This wingtip location caused troubles during the experiment: intensive vibration (apparent resonance) at ferrying speeds and altitudes resulted in sensor failures. Extensive data was only collected during RF03

and RF05, although limited data are also available on some other fights.

Water vapor. DEWPOINT HYGROMETERS. Two General Eastern Model 1011B hygrometers are routinely flown on the NSF/NCAR C130 for the purpose of obtaining airborne measurements of dewpoint and frost point temperatures. As stated by the instrument manufacturer, these sensors are capable of measuring dew-/frost points between –75° and +50°C over a wide range of temperatures, pressures, and airspeeds.

The General Eastern hygrometers operate on the chilled-mirror principle. Under this method, a mirror is thermoelectrically cooled until it reaches a temperature at which condensation begins to form. The mirror is then held at that temperature, and the presence of condensation is sensed optically. The signal output from the instrument is a voltage corresponding to the temperature of the mirror.

The accuracy of the measurements obtained from the General Eastern hygrometers is a function of the dewpoint temperature. At a dewpoint temperature of –75°C, the error in the measurements is approximately ±1.0°C. At a dewpoint temperature of +50°C, the associated error is approximately ±0.25°C. The response time of the hygrometers is variable and is de-

TABLE S3. Offset times for flight segments for RF01–RF03. Here, RL denotes remote sensing leg; CB, cloud-base leg; SC, subcloud leg; CT, cloud-top leg; SP, special pattern (which varied from flight to flight); SF, surface flux leg. For the profiles we label full profiles (FP), cloud profiles (CP), and inversion profiles (IP).

RF01 legs				RF01 profiles			
No.	GALT (m)	Time (s)	Type	No.	GALT (m)	Time (s)	Type
1	3248 ± 3.7	5550 – 7450	RL	1	3246 – 183	7490 – 8005	FP
2	625 ± 4.2	8400 – 10 200	CB	2	183 – 643	8005 – 8110	FP
3	637 ± 3.5	10 500 – 12 200	CB	3	616 – 892	10 233 – 10 310	CP
4	481 ± 3.6	12 400 – 14 200	SC	4	892 – 615	10 310 – 10 426	CP
5	492 ± 4.3	14 320 – 16 200	SC	5	494 – 915	16 210 – 16 327	CP
6	758 ± 3.3	16 600 – 18 200	CT	6	915 – 750	16 327 – 16 393	CP
7	755 ± 3.2	18 500 – 20 150	CT	7	750 – 166	20 155 – 20 419	CP
8	1056 ± 2.9	20 700 – 22 400	RL	8	166 – 1074	20 419 – 20 584	FP
9	924 ± 7.10	22 650 – 22 950	SP	9	1050 – 761	22 465 – 22 544	IP
10	152 ± 3.2	23 420 – 25 020	SF	10	761 – 945	22 544 – 22 608	IP
11	96 ± 6.4	25 200 – 27 000	SF	11	935 – 149	22 955 – 23 168	FP
12	1893 ± 3.2	27 400 – 29 200	RL	12	113 – 1920	27 060 – 27 300	FP

RF02 legs				RF02 profiles			
No.	GALT (m)	Time (s)	Type	No.	GALT (m)	Time (s)	Type
1	2598 ± 4.1	5520 – 7495	RL	1	2601 – 194	7502 – 8013	FP
2	485 ± 3.9	8900 – 11 180	CB	2	194 – 817	8013 – 8151	FP
3	517 ± 3.2	11 260 – 12 380	CB	3	765 – 431	8349 – 8471	CP
4	271 ± 4.8	12 860 – 14 750	SC	4	520 – 757	12 422 – 12 470	CP
5	271 ± 3.8	14 900 – 16 640	SC	5	758 – 198	12 469 – 12 608	FP
6	674 ± 4.5	16 975 – 18 900	CT	6	166 – 790	16 750 – 16 854	FP
7	674 ± 3.2	19 020 – 20 840	CT	7	678 – 181	20 841 – 21 020	FP
8	1117 ± 3.8	21 560 – 23 120	RL	8	838 – 84	25 177 – 25 468	FP
9	761 ± 4.6	23 30 – 25 100	SP	9	102 – 2494	27 479 – 27 804	FP
10	107 ± 5.1	25 500 – 27 440	SF				
11	2530 ± 3.0	27 860 – 29 660	RL				

pendent on the dewpoint, the slew rate, and the flow rate and thickness settings for the sensor. At higher dewpoints and moderate depressions (with depression taken as the temperature difference between the mirror and the sensor body), the response time is typically 1°C s^{-1}. At lower dewpoints and/or larger depressions, the response time can—at the upper limit—approach tens of minutes. These slower response times at low dewpoint values are also partly attributable to the reduced availability of water molecules and the resulting slow crystal growth rate. The slower response of the General Eastern hygrometers at lower dewpoints has, in fact, been routinely observed by the Research Aviation Facility (RAF). When operated in regions of the atmosphere (i.e., higher altitudes) where the ambient temperature is colder and dewpoint temperature is lower, the signals from the General Eastern hygrometers on the C130 display a much slower response and also exhibit marked oscillatory behavior.

It has been the experience of the RAF that mixing ratio values derived from the General Eastern hygrometer data show periodic "overshooting" and offsetting from mixing ratio data obtained from the RAF Lyman-alpha hygrometers. This problem typically occurs in more humid atmospheric environments and is attributable to temporary saturation of the General Eastern sensors. Thus, for those cases in which the C130 is flying in high humidity environments, users of RAF datasets are advised to rely on collected Lyman-alpha data for mixing ratio measurements.

FAST RESPONSE HYGROMETERS. Two Lyman-α probes, a new laser hygrometer (the tunable diode laser, TDL), and chilled mirror devices were used to estimate water-vapor mixing ratios. One Lyman-α was a cross-flow instrument that had a slightly slower response, but performed better in cloud; both Lyman-α probes were calibrated on-the-fly by slaving them on long timescales to the chilled-mirror dewpoint hygrometers. Initial examinations of the data indicated that the cross-flow instrument performed more reliably. The TDL is an open-path instrument that scans a water-vapor spectral line near 1.37 μm (May 1998). Test flights indicated that it performed better than the Lyman-α probes in cloud, although its performance is still being evaluated. While in the past the TDL has been sampled at 1 samples per second (sps), for DYCOMS-II it sampled the flow at a variety of rates, at times making an independent measurement every 128 ms.

Trace gas measurements (CO_2, CO, O_3, DMS). To measure in situ CO_2, a commercial nondispersive infrared analyzer was modified to implement temperature and pressure control after the manner of Boering et al. (1994). Because the NCAR instrument was developed for tropospheric measurements, water was removed from ambient samples using a Nafion dryer and a

TABLE S4. Offset times for flight segments for RF03.

RF03 legs				RF03 profiles			
No.	GALT (m)	Time (s)	Type	No.	GALT (m)	Time (s)	Type
1	2620 ± 8.4	2130 – 2860	RL	1	2612 – 164	7033 – 7455	FP
2	2613 ± 3.3	3140 – 6940	RL	2	164 – 414	7455 – 7532	FP
3	377 ± 4.2	7657 – 9330	CB	3	378 – 735	112 247 – 11 317	CP
4	378 ± 5.0	9450 – 11 192	CB	4	735 – 176	11 317 – 11 452	CP
5	192 ± 4.4	11 462 – 13 332	SC	5	194 – 743	13 332 – 13 445	CP
6	527 ± 4.7	13 537 – 15 380	CT	6	743 – 516	13 445 – 13 531	CP
7	755 ± 3.2	15 500 – 17 262	CT	7	527 – 168	17 315 – 17 425	CP
8	1092 ± 2.4	17 723 – 19 523	RL	8	162 – 1118	17 450 – 17 63	FP
9	370 ± 4.3	21 992 – 23 792	SC	9	1093 – 561	19 573 – 19 743	IP
10	97 ± 3.5	24 107 – 25 750	SF	10	687 – 233	21 454 – 21 662	IP
11	98 ± 4.3	25 900 – 27 657	SF	11	233 – 179	21 662 – 21 705	FP
12	2547 ± 3.6	28 012 – 29 898	RL	12	370 – 80	23 782 – 23 880	FP
				13	104 – 2516	27 710 – 27 992	FP

$MgClO_4$ desiccant trap. The instrument had a precision of 0.1 ppbv for a 10-s averaging time and an accuracy of ±0.4 ppbv.

The CO was measured using a commercially available instrument based on the principle of vacuum ultra violet resonance fluorescence, as published by Gerbig et al. (1999). The instrument had a 3-ppbv detection limit, for a 0.06-s averaging time, with an accuracy of ±3 ppbv.

Two methods were utilized to measure ozone. The first was based on UV absorption, and had a 0.1-Hz sample rate and a 1-ppbv detection limit. A fast response instrument was also deployed, using the chemiluminiscent reaction with NO to quantify ozone. This instrument exhibited a 3-Hz frequency response and a 0.2-ppbv detection limit.

Atmospheric pressure ionization mass spectrometry (APIMS) was used to measure DMS. In this implementation of APIMS, the reagent ion H_3O+ is formed from primary ions from ionization of nitrogen and water vapor (H_2O) by a nickel-63 beta emission. The monitored ion is DMSH+, which is formed from the reactions of DMS with H_3O+. Our use of APIMS includes the continuous addition of high isotopic purity d3-DMS as an internal standard. This results in high precision of the measurements and also allows unambiguous determination of the sensitivity of the technique as atmospheric conditions vary.

TABLE S5. Offset times for flight segments for RF04 and RF05.

RF04 legs				RF04 profiles			
No.	GALT (m)	Time (s)	Type	No.	GALT (m)	Time (s)	Type
1	2582 ± 4.2	4682 – 6757	RL	1	2549 – 183	6770 – 7395	FP
2	676 ± 3.8	7807 – 9800	CB	2	183 – 1026	7395 – 7705	FP
3	677 ± 5.3	9970 – 11 850	CB	3	1027 – 683	7703 – 7814	CP
4	368 ± 4.0	12 347 – 14 100	SC	4	679 – 1115	11 844 – 11 940	CP
5	370 ± 4.6	14 210 – 16 047	SC	5	1115 – 181	11 940 – 12 250	FP
6	1304 ± 2.7	16 562 – 18 172	RL	6	170 – 1218	16 097 – 16 362	FP
7	949 ± 3.4	18 337 – 20 100	CT	7	1301 – 933	18 174 – 18 326	IP
8	947 ± 3.1	20 272 – 22 072	CT	8	1135 – 99	23 750 – 24 150	FP
9	Porpoising	22 132 – 23 797	SP	9	105 – 2560	26 345 – 26 685	FP
10	101 ± 3.6	24 172 – 26 342	SF				
11	2518 ± 4.3	26 712 – 28 547	RL				

RF05 legs				RF05 profiles			
No.	GALT (m)	Time (s)	Type	No.	GALT (m)	Time (s)	Type
1	2578 ± 4.2	4638 – 6473	RL	1	2572 – 158	6478 – 6858	FP
2	728 ± 3.5	7412 – 8850	CB	2	158 – 975	6858 – 7068	FP
3	728 ± 3.5	8980 – 10 766	CB	3	975 – 646	7080 – 7168	CP
4	357 ± 3.4	11 300 – 12 840	SC	4	729 – 1020	10 763 – 10 830	CP
5	355 ± 3.4	12 970 – 14 700	SC	5	1020 – 154	10 830 – 11 027	FP
6	1007 ± 2.4	15 158 – 16 808	RL	6	154 – 396	11 028 – 11 088	SP
7	782 ± 3.1	17 330 – 18 680	CT	7	356 – 172	14 759 – 14 805	SP
8	784 ± 3.1	18 920 – 20 630	CT	8	136 – 1025	14 824 – 14 969	FP
9	Porpoising	20 656 – 22 349	SP	9	1010 – 736	16 801 – 16 880	IP
10	752 ± 4.7	22 463 – 24 083	CT	10	755 – 108	24 078 – 24 267	FP
11	100 ± 4.6	25 043 – 27 028	SF	11	99 – 2570	27 023 – 27 273	FP
12	2526 ± 4.4	27 348 – 28 838	RL				

During DYCOMS-II the DMS measurements were made by sampling for ambient DMS for 20 ms followed by 20 ms of the DMS standard to yield a net sampling rate of 25 Hz (sps). The detection limit is estimated to be 1 pptv for a 1-*s* integration.

Particle inlets. Inside the cabin of the C130 was a wide variety of instrumentation for measuring aerosol particles in real time and for collecting particles for later analyses. Four inlets were used to bring ambient air samples inside the cabin for particle measurements: low turbulence inlet (LTI), solid diffuser inlet (SDI), counterflow virtual impactor (CVI), and condensation nuclei (CN) cone. The LTI and SDI were operated isokinetically (velocity at the inlet tip matched the airspeed) so that ambient concentrations of large particles (> 1 μm) are preserved.

The LTI provided sample air to streaker and impactor instruments. The LTI uses boundary layer suction in the inlet tip to reduce the loss of large particles by turbulence. As a result, the concentration of large particles is enhanced in the core flow. LTI flows were controlled automatically to maintain isokinetic sampling at the inlet tip and to reduce turbulence in the diffuser inlet.

TABLE S6. Offset times for flight segments for RF07 and RF08.

RF07 legs				RF07 profiles			
No.	**GALT (m)**	**Time (s)**	**Type**	**No.**	**GALT (m)**	**Time (s)**	**Type**
1	2613 ± 2.4	7423 – 9618	RL	1	2621 – 145	9614 – 10 187	FP
2	446 ± 5.0	10 690 – 12 490	CB	2	145 – 920	10 187 – 10 473	FP
3	450 ± 3.4	12 600 – 14 400	CB	3	921 – 426	10 472 – 10 680	CP
4	231 ± 3.7	14 770 – 16 570	SC	4	444 – 973	14 400 – 14 515	CP
5	228 ± 3.5	16 741 – 18 541	SC	5	973 – 158	14 515 – 14 683	FP
6	1070 ± 3.1	18 788 – 20 598	RL	6	144 – 1090	18 563 – 18 758	FP
7	712 ± 4.4	20 708 – 22 508	CT	7	1071 – 706	20 597 – 20 728	IP
8	677 ± 5.1	22 708 – 24 500	CT	8	679 – 140	24 501 – 24 628	SP
9	Porpoising	24 773 – 25 718	SP	9	140 – 919	24 628 – 24 809	FP
10	90 ± 4.3	26 050 – 27 750	SF	10	902 – 85	25 641 – 25 915	FP
11	100 ± 3.2	27 990 – 29 790	SF	11	97 – 2564	29 796 – 30 127	FP
12	1553 ± 4.1	30 190 – 32 010	RL				

RF08 legs				RF08 profiles			
No.	**GALT (m)**	**Time (s)**	**Type**	**No.**	**GALT (m)**	**Time (s)**	**Type**
1	5695 ± 5.3	5839 – 7680	RL	1	5694 – 136	7675 – 8741	FP
2	437 ± 1.9	9158 – 10 908	CB	2	136 – 569	8741 – 8848	FP
3	472 ± 2.2	11 000 – 12 824	CB	3	604 – 417	8923 – 9053	CP
4	135 ± 2.4	13 184 – 14 924	SF	4	467 – 640	12 818 – 12 908	CP
5	255 ± 2.2	15 043 – 16 938	SC	5	637 – 126	13 003 – 13 168	FP
6	1067 ± 2.9	17 378 – 19 058	RL	6	253 – 61	16 942 – 16 997	SP
7	Porpoising	19 199 – 20 999	SP	7	61 – 913	16 997 – 17 172	FP
8	90 ± 2.9	21 195 – 23 013	SF	8	1068 – 476	19 059 – 19 182	IP
9	275 ± 2.9	23 273 – 24 908	SC	9	542 – 94	21 016 – 21 177	FP
10	495 ± 2.6	25 238 – 26 908	CB	10	269 – 720	24 903 – 25 038	CP
11	524 ± 2.9	27 112 – 28 417	CT	11	720 – 499	25 038 – 25 113	IP
12	2583 ± 3.3	28 838 – 32 338	RL	12	526 – 185	28 418 – 28 485	SP
				13	185 – 2606	28 485 – 28 818	FP

The SDI provided air for cloud condensation nuclei (CCN), optical particle counter, and CN measurements, independent of the LTI. The SDI is a conical diffuser that decelerates the flow from 110 to 4 m s^{-1}. Flow rates for isokinetic sampling with the SDI were calculated over a range of airspeeds typical for the C130. Flow demands of the instruments were normally fixed, and isokinetic sampling was achieved for airspeeds of 113 m s^{-1}. Nonisokinetic sampling occurred when the aircraft speed was different from this or during occasional interruptions for changing sample media or servicing instruments.

Aerosol particle collections. Aerosol particle samples were collected from the LTI, SDI, and CVI. Some particles were collected on Nucleopore filter substrate, while others were simultaneously impacted on electron microscope grids. The particle samples were analyzed for physicochemical properties by scanning and transmission electron microscopy (SEM and TEM, respectively) and elemental single-particle analysis methods (Anderson et al. 1996; Twohy and Gandrud 1998).

High volume air flow from the SDI fed a three-stage virtual impactor in which the concentration of particles was increased by a factor 23 into sequentially smaller flows. The final highly concentrated sample was collected on stretched Teflon filters. This technique produces sufficient mass for sensitive analyses in a relatively short time. These teflon filter samples of submicron particles and some CVI droplet residue particles were analyzed for organic and inorganic functional groups by Fourier transform infrared (FTIR) spectroscopy (Allen et al. 1994) and for elemental analysis by X-ray fluorescence (XRF).

Microphysical and particle instrumentation. LIQUID-WATER PROBES. A great variety of probes were flown for estimating properties of particles (including cloud droplets) in the STBL. To estimate bulk properties of the cloud layer, such as liquid-water, two Particle Measuring Systems, Inc. (PMS) King probes and a PVM-100A were available. The King probe is based on a hot-wire technique that measures the liquid-water concentration in the range of 0.05–3 g m^{-3}; it samples a volume of 4000 cm^s s^{-1} at 10 sps. The PVM-100A is a very high rate instrument that uses a light scattering technique to estimate integrated droplet distribution volume and surface area for drops larger than 4-μm diameter. This instrument samples a volume of 300 cm^3 s^{-1} at a rate of up to 1000 sps. During flights RF01 and RF02 the PVM-100A sampled the flow at a rate of 250 sps, on subsequent flights it sampled at 1000 sps.

A complementary instrument, the Cloud Integrating Nephelometer (CIN) measures in situ the optical scattering coefficient of cloud particles with sizes over a range of about 5–2000 μm in diameter. Its sample volume is 0.3 m^3 s^{-1} and data are sampled at a rate of up to 250 sps. Its sensitivity to a wide size range of particles covers the individual size ranges of other microphysics probes used on the C130, such as the SPP-100 droplet probe and the 260X drizzle probe, making it possible to perform data consistency checks that may enhance data accuracy.

OPTICAL PARTICLE PROBES. To estimate the distribution of particles at a given size a number of techniques and probes were used as outlined in Table S7. The probes operated using one of several basic principles, single-particle scattering (sps) or shadowing of light. The scattering of the SPP-100 and FFSSP is calibrated assuming water scatterers. The SPP-200 and SPP-300 are calibrated using beads with a refractive index of 1.59. The SPP family of probes is derived from earlier versions from PMS, with upgraded electronics from Droplet Measurement Technologies.

RDMA. The Radial Differential Mobility Analyzer (RDMA) measures the size distribution and concentration of particles in the size range 8–130-nm diameter (Russell et al. 1996). The technique is to put an electrical charge on particles in the sample air and then to pass the sample through a small chamber that has a continuous flow of dry, particle-free sheath air. The flows of sample and sheath flow are precisely controlled at 8.3 and 83 cm^3 s^{-1}, respectively. Narrow size segments of the particles are extracted by imposing an electrical field perpendicular to the air flow, and these particle are passed to a CN counter. Every 3 min, the voltage cycles through a smooth exponential curve from 0–5000 V and back to 0 V. The time histories of particle counts, voltages, and flows are numerically inverted to generate upscan and downscan size distribution measurements, $dn/d\log D_p$ versus particle diameter D_p, in 62 bins. Size calibrations were done with 80-nm monodisperse polystyrene latex spheres. Sample air for the RDMA came from the starboard side solid-diffuser inlet. The RDMA performed well during all of the DYCOMS-II flights. A new bulk cloud water collection system jointly developed at Colorado State University (CSU) and the National Center for Atmospheric Research was mounted on the starboard instrumentation pod (Fig. S4). It provided bulk cloud water samples for chemical characterization and cloud processing studies.

Table S7. Instruments for in situ measurements of cloud and aerosol particle size distributions.					
Instrument	Range (μm)	Sample volume (cm^{-3} s^{-1})	Principle	Feature (frequency, channels)	Operator
SPP-200	0.1–3	1	SPS	10 Hz, 30	RAF
SPP-300	0.3–30	7	SPS	10 Hz, 30	RAF
SPP-100	2–47	50	SPS-water	10 Hz, 40	RAF
F-FSSP	5–44	50	SPS-water	asynchronous 255	Brenguier
PMS-260X	10–640	4000	Shadow	10 Hz, 60	RAF
PMS-2DC	25–800	5000	Shadow	10 Hz, 32	RAF

CCN AND CN INSTRUMENTS. Two Wyoming CCN counters (WyoCCN) were flown during DYCOMS-II. WyoCCN is a static thermal-gradient diffusion chamber, taking a grab sample every 30 s. Both the top and the bottom plates of the chamber are covered with water-saturated blotter paper. A temperature controller regulates the differential temperature between the plates, thus creating a supersaturation in the center of the chamber. Particles with critical supersaturation less than the controlled supersaturation activate and grow to the size of cloud droplets. These are illuminated by a laser and the scattered light intensity is recorded. [For a detailed description of the WyoCCN instrument see Delene and Deschler (2000).] Both instruments measured CCN number concentration at supersaturations of 0.2%, 0.4%, 0.8%, and 1.6%. In addition, two continuous flow CN counters (TSI 3010 and TSI 3760)[2] measured the concentration of particles larger than 0.01 μm.

CLOUD WATER COLLECTOR. The cloud water collection system employs an axial-flow cyclone to separate cloud droplets from the ambient airstream. At flight speeds (110 m s^{-1}), ram pressure drives air and cloud droplets into the 6-cm diameter inlet of the axial-flow cyclone. A stationary curved vane assembly redirects the incoming axially directed flow to produce a rapidly rotating flow field. In this flow, centrifugal force rapidly moves entrained cloud droplets to the wall of the collector. Accumulated cloud water is drawn off the wall of the collector and directed to a sample storage system consisting of seven storage bottles that are filled sequentially during a flight. The entire cloud water collection system is housed in a PMS canister and is operated with a LabVIEW-based control and data acquisition system.

A computational fluid dynamics (CFD) analysis of the axial-flow cyclone provided a prediction of collector performance, and indicated a 50% cut diameter of approximately 8 μm when operated at 115 m s^{-1}. Over the course of the project 54 samples were obtained. Sample pH was measured on site immediately following each flight, and the cloud water from each sample period was preserved on site for postcampaign analysis at CSU. Concentrations of major ions (Cl^-, NO_3^-, SO_{42}^-, Na^+, NH_4^+, K^+, Ca_2^+ and Mg_2^+), peroxide, formaldehyde, S(IV), and trace metals have been measured. Preliminary analysis indicates that sodium and chloride were the two most abundant ions in every DYCOMS-II sample, accounting for approximately two-thirds of the total ions in the solution. Ratios of chloride, potassium, magnesium, and calcium to sodium show that these species were present in proportions similar to those found in seawater. Sulfate, nitrate, and ammonium had ratios that were higher than what would be expected in seawater, indicating that there were additional sources for these species in the remote marine environment.

COUNTERFLOW VIRTUAL IMPACTOR (CVI). The CVI (Noone et al. 1988; Twohy et al. 1997) has been utilized both in the air and on the ground in studies of aerosol–cloud interactions, cloud physics, and climate. For DYCOMS-II, it was used to compare properties of material within droplets to properties of ambient aerosol particles in order to study which particles nucleate clouds and how clouds process particles. At the CVI inlet tip, cloud droplets larger than about 8-mm aerodynamic diameter were separated from the interstitial aerosol and impacted into dry nitrogen. This separation is possible via a counterflow stream of nitrogen out of the CVI tip, which assures that only cloud droplets (with more inertia) are sampled. The water vapor and nonvolatile residual

[2] TSI 3010 was operated by the University of Wyoming; TSI 3760 was operated by NCAR.

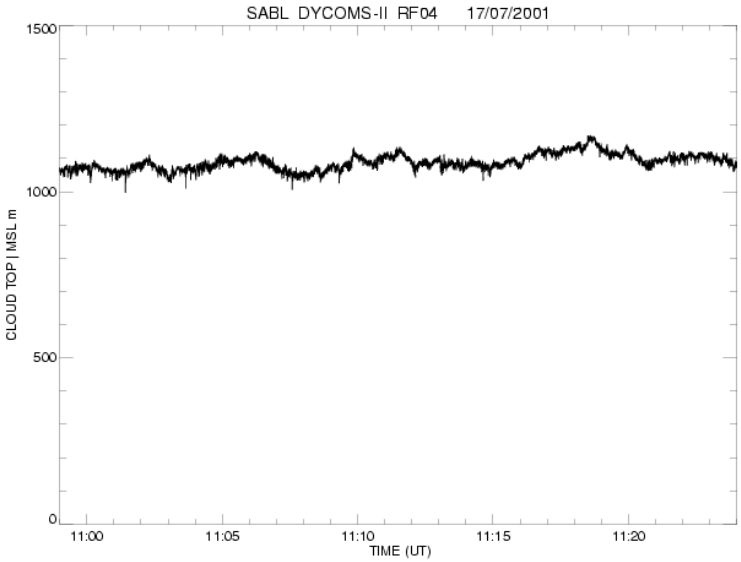

Fig. S6. Cloud top derived from SABL on RF04.

particles remaining after droplet evaporation are sampled downstream of the inlet with selected instruments. In DYCOMS-II, these included a CN counter and optical particle counter to measure residual particle number and size distribution, electron microscope samples for single particle chemical analysis, filters for FTIR/XRF analysis of organic functional groups and elements, and a Lyman-α hygrometer for liquid water content.

Remote Sensors. Wyoming cloud radar (WCR). The WCR (information online at www-das.uwyo.edu/wcr) was operated with a dual-antenna arrangement, one antenna pointing vertically down (the nadir beam), the other at a 38° backward slant in the plane defined by the aircraft axis and the nadir beam. The two antennas were used in a rapidly interleaved fashion. Data so obtained will yield dual-Doppler analyses. The radar was operated during all flights. The radar legs (RL in Table S3) flown not far above cloud top yielded full coverage from the ocean surface to the top of the cloud. Flight segments in and below the cloud layer provided partial views. Flight segments at altitudes > 2 km yielded poor data because of the loss in sensitivity with distance to the target.

The WCR spatial resolution is 30 m but the sampling/recording was done with 15-m spacing. The minimum detectable signal (with high signal to noise ratio) at 300-m distance to the target was about –26 dB*Z*. This sensitivity was sufficient to yield measurements even in the most tenuous of the clouds encountered during DYCOMS-II.

The WCR recorded data in over 90% of the total flight times. In two flights (RF06 and RF09), the flight plan was designed to give maximum temporal resolution in repeated sampling of the same cloud volume.

Scanning Aerosol Backscatter Lidar (SABL). SABL is an elastic backscatter lidar that was used to map atmospheric backscatter and cloud-edge structure. The lidar has a Nd:YAG laser as the source operating at 20 Hz and at two wavelengths: 1064 and 532 nm. SABL is mounted in an NCAR/RAF instrumentation pod on the left wing and is capable of looking vertically either up or down. The return signals from both wavelengths are digitized with a 12-bit digitizers at rates up to 40 MHz. Cloud-top height is obtained from the remote sensing flight legs when the aircraft was more than 200 m from the cloud. Even though the detectors are saturated by the cloud return from close range, the range to the cloud top or cloud bottom can still be extracted from the return signal. Figure S6 is plot of cloud-top height versus time from RF04 during a remote sensing leg of the flight. Cloud-top information is obtained from individual profiles so the horizontal spacing between profiles is approximately 5 m. The 40-MHz digitization rate gives a vertical resolution of 3.75 m.

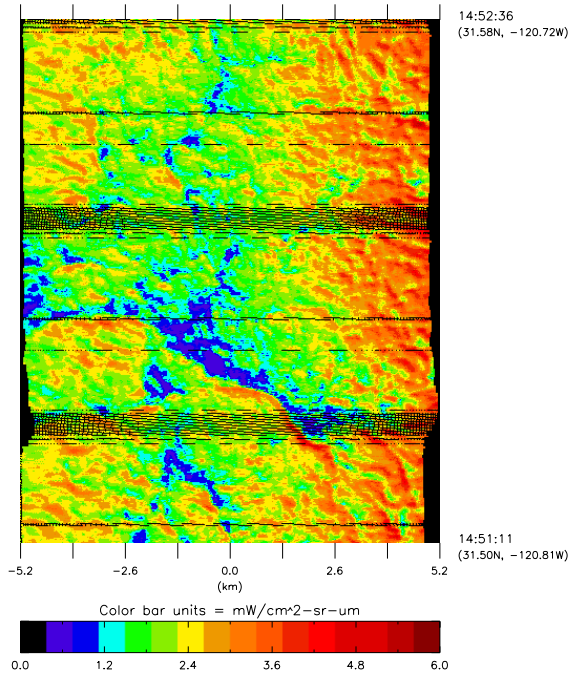

Fig. S7. MCR channel 4 from RF02.

Table S8. Specifications for MCR.

Channel	$\lambda(\mu m)$	$\Delta\lambda_{FW\,HM}$ (μm)	Application
1	0.640	0.063	τ and cloud mapping
2	0.761	0.001	
3	0.763	0.001	
4	1.06	0.07	r_e
5	1.64	0.05	Phase
6	2.16	0.08	Phase and particle size
7	10.9	0.9	Not operating

Table S9. Specifications for Heimann KT 19.85 pyrometer.

Passband	9.6–11.5 μm
Range	–50 to 400°C
Resolution	≈ 1°C (depending on surface temperature)
Response time	0.3 s (adjustable)
Field of view	2°

Table S10. Satellite datasets.

Platform	Sensor types	Data types
GOES	Imager and sounder	Binary data and images
NOAA	AVHRR, AMSU, HIRS, SSU, MSU	Binary data and images
DMSP	SSM/I and Visible/Infrared Sensor	Binary data and images
QuikSCAT	Scatterometer	Binary data
ERS-1	Scatterometer	Images
TRMM	Microwave Imager	Binary data
Terra	MODIS	Binary data

Multichannel Cloud Radiometer (MCR). The MCR is a seven-channel radiometer that scans between ±45° about the flight track with a mirror scan rate of 3.47 revolutions per second. Data from each channel are simultaneously sampled with an overall rate of 5000 sps. Each active scan yields 360 samples (pixels), with pixel sizes depending on height above target; swaths widths are roughly twice the distance to the target. Since the scanning is continuous, the MCR produces a spectrally resolved image (see for instance Fig. S7) of features below the aircraft, including cloud tops, terrain, vegetation, pack ice, etc. Channel 7 (Table S8) is in the infrared and it was hoped that it would provide nocturnal imaging of the cloud layer; however, this channel did not function properly and images are limited to the daytime, and thus only the early morning periods at the end of nocturnal flights are available.

Pyrometers. Two EG&G Heimann Optoelectronics radiation pyrometers are routinely deployed on the NSF/NCAR C130 for the purpose of obtaining airborne surface temperature measurements. The RAF uses Heimann model KT 19.85 pyrometers (see specifications in Table S9), which operate in the spectral range of 9.6–11.5 μm. The latter is a portion of the electromagnetic spectrum in which atmospheric transmission is high. Consequently, the KT 19.85 pyrometers are, for the most part, well suited for making surface temperature measurements on board research aircraft. Certain environmental effects can degrade the accuracy of surface temperature measurements obtained from Heimann pyrometers flown on aircraft. Specifically, potential errors can be introduced into surface temperature measurements obtained using these pyrometers by 1) nonunity emittance and nonzero reflectance of the ground or sea surface being studied and 2) the emission of infrared (IR) radiation by water vapor in the atmospheric layer between the pyrometer and the surface. (Additional discussion of these two phenomena and on the Heimann KT 19.85 pyrometers in general can be found online: http://raf.atd.ucar.edu/Bulletins/bulletin25.html.)

Calibration of the Heimann pyrometers is carried out periodically in the RAF calibration laboratory using an Eppley Laboratories Inc., Infrared Blackbody Source Model BB16T. This blackbody target displays a temperature accuracy and uniformity of 0.1°C over a temperature range of 10° to 60°C and has an emissivity of 0.995.

Satellites. Various satellite data, which were collected as part of the study, are tabulated in Table S10.

REFERENCES

Allen, D. T., E. J. Palen, M. I. Haimov, S. V. Hering, and J. R. Young, 1994: Fourier-transform infrared-spectroscopy of aerosol collected in a low-pressure impactor (lpi/ftir)—Method development and field calibration. *Aerosol Sci. Technol.,* **21,** 325–342.

Anderson, J. R., P. R. Buseck, and R. Arimoto, 1996: Characterization of the Bermuda aerosol by combined individual-particle and bulk-aerosol analysis. *Atmos. Environ.,* **30,** 319–338.

Boering, K. A., B. C. Daube Jr., S. C. Wofsy, M. Loewenstein, J. R. Podolske, and E. R. Keim, 1994: Tracer–tracer relationships and lower stratospheric dynamics: CO_2 and N_2O correlations during SPADE. *Geophys. Res. Lett.,* **21,** 2567–2570.

Brown, E. N., C. A. Friehe, and D. H. Lenschow, 1983: The use of pressure fluctuations on the nose of an aircraft for measuring air motion. *J. Climate Appl. Meteor.,* **22,** 171–180.

Cooper, W. A., and D. Rogers, 1991: Effects of airflow trajectories around aircraft on measurements of scalar fluxes. *J. Atmos. Oceanic Technol.,* **8,** 66–77.

Delene, D. J., and T. Deschler, 2000: Calibration of a photometric cloud condensation nucleus counter designed for deployment on a baloon package. *J. Atmos. Oceanic Technol.,* **17,** 459–467.

Friehe, C. A., 1986: Fine scale measurements. *Probing the Atmospheric Boundary Layer,* D. H. Lenschow, Ed., Amer. Meteor. Soc., 29–38.

Gerbig, C., S. Schmitgen, D. Kley, A. Volz-Thomas, K. Dewey, and D. Haaks, 1999: An improved fast-response vacuum–UV resonance fluorescence CO instrument. *J. Geophys. Res.,* **104** (D1), 1699–1704.

Haman, K. E., A. Makulski, and S. P. Malinowski, 1997: A new ultrafast thermometer for airborne measurements in clouds. *J. Atmos. Oceanic Technol.,* **14,** 217–227.

Kayton, M., and W. R. Fried, 1997: *Avionics Navigations Systems.* Wiley, 773 pp.

Lenschow, D. H., 1972: The measurement of air velocity and temperature using the near Buffalo aircraft measuring system. NCAR Tech. Note EDD-74, 39 pp.

——, 1986: Aircraft measurements in the boundary layer. *Probing the Atmospheric Boundary Layer,* D. H. Lenschow, Ed., Amer. Meteor. Soc., 39–55.

——, and W. T. Pennell, 1974: On the measurement of in-cloud and wet-bulb temperatures from an aircraft. *Mon. Wea. Rev.,* **102,** 447–454.

May, R. D., 1998: Open-path, near-infrared tunable diode laser spectrometer for atmospheric measurements of H_2O. *J. Geophys. Res.,* **103,** 19 161–19 172.

Noone, K., J. A. Ogren, J. Heintzenberg, R. J. Charlson, and D. S. Covert, 1988: Design and calibration of a counterflow virtual impactor for sampling of atmospheric fog and cloud droplets. *Aerosol Sci. Technol.,* **8,** 235–244.

Russell, L. M. S.-H. Zhang, R. C. Flagan, J. H. Seinfeld, M. R. Stolzenburg, and R. Caldow, 1996: Radially classified aerosol detector for aircraft-based submicron aerosol measurements. *J. Atmos. Oceanic Technol.,* **13,** 598–609.

Spyers-Duran, P., and D. Baumgardner, 1983: In flight estimation of time response of airborne temperature sensors. Preprints, *Fifth. Symp. on Meteorological Observations and Instrumentation,* Toronto, ON, Canada, Amer. Meteor Soc., 237–255.

Twohy, C. H., and B. W. Gandrud, 1998: Electron microscope analysis of residual particles from aircraft contrails. *Geophys. Res. Lett.,* **25,** 1359–1362.

——, A. J. Schanot, and W. A. Cooper, 1997: Measurement of condensed water content in liquid and ice clouds using an airborne counterflow virtual impactor. *J. Atmos. Oceanic Technol.,* **14,** 197–202.